

# Graded-index fiber lens proposed for ultrasmall probes used in biomedical imaging

Youxin Mao,\* Shoude Chang, Sherif Sherif, and Costel Flueraru

Institute for Microstructural Sciences, National Research Council Canada, 1200 Montreal Road, Ottawa, K1A 0R6, ON, Canada

\*Corresponding author: Linda.Mao@nrc-cnrc.ca

Received 17 January 2007; revised 5 April 2007; accepted 20 June 2007;  
posted 20 June 2007 (Doc. ID 79136); published 9 August 2007

The quality and parameters of probing optical beams are extremely important in biomedical imaging systems both for image quality and light coupling efficiency considerations. For example, the shape, size, focal position, and focal range of such beams could have a great impact on the lateral resolution, penetration depth, and signal-to-noise ratio of the image in optical coherence tomography. We present a beam profile characterization of different variations of graded-index (GRIN) fiber lenses, which were recently proposed for biomedical imaging probes. Those GRIN lens modules are made of a single mode fiber and a GRIN fiber lens with or without a fiber spacer between them. We discuss theoretical analysis methods, fabrication techniques, and measured performance compared with theory. © 2007 Optical Society of America

OCIS codes: 170.4500, 170.3880, 170.3890, 170.3660, 060.2350.

## 1. Introduction

Optical biomedical imaging techniques, such as optical coherence tomography (OCT) [1] and Doppler OCT [2,3], are becoming increasingly important tools for both diagnosis and guided surgery because of their high image resolutions. OCT can provide images on the cellular level whereas Doppler OCT can detect blood flow with velocity sensitivities approaching a few micrometers per second [4,5]. However, in most optically nontransparent tissues, OCT has a typical imaging depth limitation of 1–3 mm. Similarly, Doppler OCT systems suffer from limitations where blood flow can rarely be detected beyond 1–2 mm from the tissue surface without *a priori* velocity profile information and digital extrapolation algorithms. As a result, the earliest *in vivo* OCT imaging of tissue microstructure and microvasculature was restricted to a few transparent or superficial organ sites, such as the retina [6,7] and skin [8,9]. To overcome this depth limitation, optical probes, such as endoscopes, catheters, and needles have been investigated for *in vivo* OCT imaging in mucosal layers

of the gastrointestinal tract [10,11], deep organs and tissues [12,13], and interarterial and intravascular [14,15]. However, for the imaging of small lumen, narrow space, and deep tissue and organs of humans and small animals, a key concern is the possible damage from the mechanical insertion of the optical probe. Therefore it is critical to develop an ultrasmall optical probe that is compatible with the current optical biomedical imaging systems, which results in minimum tissue damage.

*In vivo* optical imaging of internal tissues is generally performed using a fiber-optic probe, since an optical fiber can be easily and cheaply produced with a diameter of less than 150  $\mu\text{m}$ . The key components of such optical fiber probe include a small lens and a beam director, where both provide a focused optical beam directing it to a location of interest through a guide wire. Traditionally, this type of small optical probe has been implemented by attaching a small glass graded-index (GRIN) or SELFOC lens (250–500  $\mu\text{m}$ ) and a glass microprism to a single mode fiber (SMF) with optical adhesive or optical epoxy [12]. However, the gluing of a separate small lens and a tiny prism to a fiber is a complex fabrication process that results in a low quality optical interface.

A new probe design that uses optical fiber lenses, e.g., fiber GRIN lens or fiber ball lens, has recently been proposed [16]. The main advantages of fiber lenses over conventional glass lenses are their small size, ability to autoalign to a fiber, thus creating a fusion-spliced interface with low loss, low backreflection, and high mechanical integrity. The GRIN fiber lens is preferred over a ball lens because of its common or near common fiber/lens diameter. It also allows an index-matching fluid to fill the space between the lens and the probe housing because GRIN materials perform the light bending within the GRIN medium itself, thus minimizing any false images from reflections between the lens surface and the optical window. Furthermore, a beam director can be fusion spliced directly to the GRIN lens fiber. The beam director of a GRIN lens can be polished to an angle with less requirement of the depth polish tolerance, compared to a ball lens [13], to obtain a symmetric beam profile.

The quality of the beam of a fiber-optic probe is crucial for the imaging system. Ideal characteristics of a fiber-optic probe include a high Gaussian beam intensity profile, an appropriate intensity–distance shape, high flexibility, and low optical aberration and loss. To date, no paper has compared in detail the actual optical performance of a GRIN fiber based optic probe with theoretical results. Swanson *et al.* proposed the GRIN fiber based optic probes design, but presented the variations of probe structure instead of the characteristics of their performance [16]. Reed *et al.* demonstrated the usage of such probes with emphasis on their insertion loss only [17]. Both Jafri *et al.* [18] and Li *et al.* [19] reported OCT images without detailed characterization of the used GRIN lens based probes.

In this paper, we discuss theoretical analysis methods and fabrication techniques of GRIN fiber based optic probes. We compare in detail measured performance with expected theoretical performance.

## 2. Theory

For most optical imaging systems, light is guided through a SMF and focused on a sample using a lens. Backreflected light carrying information about the sample is coupled back into the fiber, and then signal detection and data processing systems will collect the useful information for imaging. The optical probe is one of the crucial parts of such an optical imaging system. The beam shape, i.e., working distance (focal distance from lens surface), depth of field (two times the Raleigh range), and spot size (waist diameter) of the optical probe in the sample will directly determine properties of the image such as image location, depth, and resolution. Thus, image quality and light coupling efficiency from the sample will be directly influenced by the beam quality of the probe. For the best optical performance of a probing lens, its beam profile must be designed to be consistent with the light penetration depth in the sample. In most biomedical imaging systems, light from the probe will be directed into a turbid tissue. Based on interaction

properties of light with turbid tissue [20], the range of penetration depth is from 0.5–3 mm at near-infrared wavelengths. For example, the penetration depths are 0.7 mm and 3.0 mm in human skin and liver, respectively, at 1300 nm, a conventional wavelength used in OCT systems. Thus, for designing an optical probe, working distance should be in the range of 0.4–1.2 mm in the air that depends on the tissues to be tested. There is a tradeoff between the depth of field and beam spot size because the depth of field of a lens is positively related to the square of the spot size according to the theory of a Gaussian beam. A large depth of field unavoidably results in a large spot size. Thus, the optimal depth of field is in the range of 0.8–1.5 mm in the air; this keeps the spot size in the range of 26–35  $\mu\text{m}$  at the 1300 nm wavelength. For an ultrasmall optical lens (diameter  $<150 \mu\text{m}$ ), it is not possible to achieve a large working distance by directly attaching a GRIN fiber lens to a SMF because of the strong focus ability of the lens and the small mode field diameter (MFD) of the SMF. A fiber spacer with a homogeneous index of refraction has to be added between the SMF and the lens for beam expansion prior to focusing to obtain a longer working distance. Therefore, theoretical analysis becomes necessary to obtain a lens design with optimized optical beam performance for imaging different tissues.

Precisely calculating the theoretical beam profile of a GRIN lens is not an easy task because of its index profile aberrations. The lack of accurate and complete lens data of GRIN fibers, compared to conventional glass GRIN lenses, makes the modeling of a GRIN fiber lens more difficult. In such a case, the accuracy of a theoretical analysis method should be judged more by experimental results rather than by theory alone. In this study, we first used a complex beam parameter Gaussian matrix transformation method [21], and then, we used the commercially available numerical optical modeling software, ZEMAX (ZEMAX Development Corporation, Washington, USA), with the same lens index profile for comparison.

From the method of ray matrix transformation of the complex beam parameter, if  $R(z)$  is the radius of curvature of a Gaussian beam and  $\omega$  is the beam waist, the complex beam parameter  $q(z)$  is given by [21]

$$\frac{1}{q(z)} = \frac{1}{R(z)} - i \frac{\lambda}{n\pi\omega^2}, \quad (1)$$

where  $\lambda$  is the free-space wavelength and  $n$  is the refractive index of the medium. The transformation of  $q(z)$  from an input plane  $q_1$  to an output plane  $q_2$  is represented by

$$q_2 = \frac{M_{0,0}q_1 + M_{0,1}}{M_{1,0}q_1 + M_{1,1}}, \quad (2)$$

where  $q_1$  is a known factor and can be expressed from Eq. (1) by inputting beam waist conditions,  $R \rightarrow \infty$

and  $\omega = \omega_0$  (i.e., half MFD of SMF),

$$q_1 = i \frac{\lambda}{n\pi\omega_0^2}. \quad (3)$$

$M = |M_{i,j}| (i, j = 0, 1)$  is the ray matrix between the input plane and the output plane (i.e., matrix of the lens system). The matrix of a GRIN fiber lens can be given by its refractive index profile, which is very similar to that of a conventional GRIN (or SELFOC) lens, i.e., a radial index gradient. The index of refraction is highest in the center of the lens and decreases with radial distance from the axis. The following quadratic equation closely describes the refractive index of a GRIN fiber lens [21]:

$$n(r) = n_0 \left( 1 - \frac{g^2}{2} r^2 \right), \quad (4)$$

where  $r$  is the radial position from the axis,  $n_0$  is refractive index on the lens axis, and  $g$  is the gradient constant given by the manufacturer. The pitch,  $p = 2\pi/g$ , is the spatial frequency of the ray trajectory. The ray matrix  $M$  of a GRIN fiber lens system shown in Fig. 1(a) can be expressed as

$$M = \begin{pmatrix} \cos(gL) & \frac{n_{\text{SMF}}}{n_0 g} \sin(gL) \\ -\frac{n_0 g}{n_2} \sin(gL) & \frac{n_{\text{SMF}}}{n_2} \cos(gL) \end{pmatrix} \times \begin{pmatrix} 1 & L_0 \\ 0 & 1 \end{pmatrix}, \quad (5)$$

where  $L$  and  $L_0$  indicate, respectively, the lengths of the GRIN fiber and the fiber spacer that is between the SMF and the GRIN fiber lens shown in Fig. 1(a).

The working distance,  $\text{Dist}$ , and Rayleigh range,  $Z_0$ , can be obtained by respectively equating the real

and image parts of the complex output beam parameter  $q_2$  from Eq. (2), and the true beam waist  $W$  can be expressed from the Rayleigh range,  $Z_0$ , as shown below:

$$\text{Dist} = \text{Re}(q_2), \quad Z_0 = \text{Im}(q_2), \quad W = \sqrt{\frac{\lambda Z_0}{n\pi}}. \quad (6)$$

The beam parameters,  $\text{Dist}$ ,  $Z_0$ , and  $W$ , can be directly calculated by the matrix equations (6), which are relatively simple calculation methods in comparison to those described in Ref. [22].

### 3. Methods

Our GRIN fiber lens modules were made from a standard Corning SMF-28 single mode fiber as the principal light guide with a no-core-fiber (NCF) as the fiber spacer and a GRIN fiber as the focusing lens. The NCF was fusion spliced via arc welds to the Corning SMF-28 and then accurately cleaved to a theoretically determined length. The GRIN fiber was then fusion spliced to the cleaved NCF and precisely cleaved at a precalculated length to generate a desired beam–distance profile (i.e., working distance, depth of field, and spot size). To ensure minimum backreflection, the indices of the NCF and the center of GRIN fiber were matched to the core index of the SMF. For a short working distance probe, the section of the NCF was omitted, resulting in a simple fabrication process.

In this paper, two types of optical GRIN fiber were investigated as an ultrasmall lens for the ultrasmall optical probe. One had a 50  $\mu\text{m}$  core size and 125  $\mu\text{m}$  outer diameter with a core refractive index  $n_0 = 1.486$  and a gradient constant  $g = 5.50$  at 1300 nm (Optical Fiber Solution, New Jersey, USA). The other fiber had a 100  $\mu\text{m}$  core size and 140  $\mu\text{m}$  outer diameter with a core refractive index  $n_0 = 1.487$  and a gradient constant  $g = 3.76$  at 1300 nm (Prime Optical Fiber Corporation, Taiwan). They are both conventional low cost off-the-shelf optical multimode GRIN fibers. The NCF (Prime Optical Fiber Corporation, Taiwan) is made of pure silica without a core but with the same cladding diameter of an SMF. Fusion splicing was processed using an Ericsson FSU 995 fusion splicer and an EFC11 fiber cleaver (3SAE Technologies, Tennessee, USA). The spliced interfaces produced minimum backreflections since the mechanical strength at the interface was similar to that of the untreated fiber. This design diminished false images from the reflections of the lens surface and the optical window by allowing the index-matched fluid to fill the space in between, which is not possible by using a ball lens. The desired focused beam profile was obtained by tailoring the length of the NCF and GRIN fibers based on the theoretical results. In order to facilitate a comparison, samples with 0, 0.36 mm, and 0.48 mm lengths of NCF were fabricated for the GRIN fibers. Information concerning the samples used in this study are listed in Table 1, including the sample number,

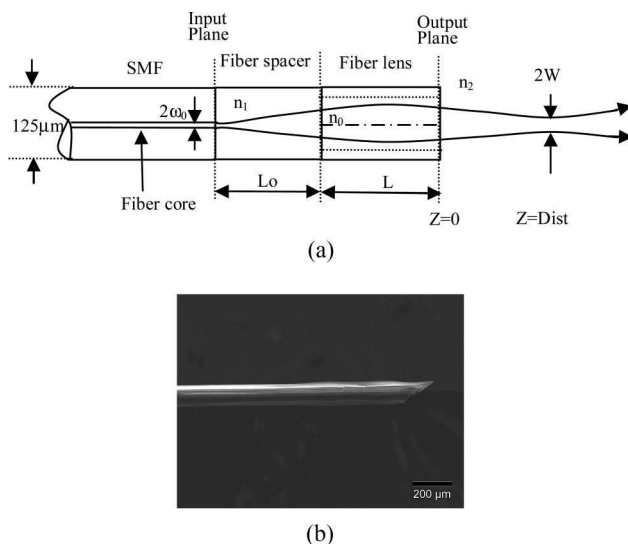


Fig. 1. (a) Typical schematics of the single mode graded index (GRIN) fiber lens system. (b) Scanning electron micrograph of a GRIN fiber lens tip attached with an angle-polished fiber prism.

Table 1. Various Sample Structures with Measured Beam Properties

Samples	Length of Coreless Fiber (mm)	GRIN Fiber Lens			Measured Beam Properties		
		Type	Length (mm)	Pitch	Working Distance (mm)	Depth of Field (mm)	Spot Size ( $\mu\text{m}$ )
1	0	50/125	0.41	0.36	0.11	0.17	13
2	0	50/125	0.33	0.29	0.16	0.45	19
3	0	50/125	0.31	0.27	0.08	0.63	22
4	0	100/140	0.60	0.36	0.18	0.16	13
5	0	100/140	0.55	0.33	0.20	0.30	16
6	0	100/140	0.52	0.31	0.28	0.50	22
7	0	100/140	0.50	0.30	0.38	0.60	23
8	0	100/140	0.48	0.29	0.41	0.85	25
9	0	100/140	0.46	0.28	0.40	1.30	30
10	0	100/140	0.45	0.27	0.38	1.45	32
11	0.36	50/125	0.12	0.11	0.50	0.60	23
12	0.36	50/125	0.11	0.10	0.60	0.9	28
13	0.36	50/125	0.10	0.09	0.65	1.1	31
14	0.36	50/125	0.09	0.08	0.63	1.2	34
15	0.36	100/140	0.21	0.13	0.65	0.7	25
16	0.36	100/140	0.20	0.12	0.9	1.1	30
17	0.36	100/140	0.18	0.11	0.8	1.6	38
18	0.48	100/140	0.17	0.102	1.00	0.95	28
19	0.48	100/140	0.16	0.096	1.10	1.5	35
20	0.48	100/140	0.145	0.087	1.20	1.8	41
21	0.48	100/140	0.14	0.084	1.05	2.0	45

length of the NCF, and type, length, and pitch of the GRIN fiber.

A beam profile measurement system (BeamView Analyzer, Oregon, USA) with an infrared camera (Electrophysics, New Jersey, USA) and a superluminescent diode source (Covega, Maryland, USA) with 60 nm 3 dB bandwidth at 1310 nm center wavelength was used to characterize the beam parameters of the lens system. A 40 $\times$  JIS (Japanese industrial standard) microscopic objective lens and a related objective tube were attached to the input window of the camera to increase the image resolution. The horizontal and vertical resolutions of the system were 1.0  $\mu\text{m}$  and 1.1  $\mu\text{m}$ , respectively. The distribution of light intensity at various distances along the direction of propagation after the lens was accurately measured by the beam profile system. Working distance, depth of focus,  $1/e^2$  spot size, and Gaussian fitting were analyzed from the measured intensity distribution. The results demonstrated in this paper are all in the air medium.

In addition, after characterization of the lens, another NCF could be fusion spliced to the lens tip as a beam director by polishing the end of the NCF to a 45 degree angle and coating the polished surface with a total reflection film. This then allowed the beam to be reflected at a 90 degree angle creating a side-view probe. Figure 1(b) shows a typical scan electron microscope (SEM) picture of the GRIN fiber lens tip with a fiber beam director. The fiber lens tip together with a tubing system and a connected linearly scanning or 360 degree rotated motor could be built as an endoscope or a needle probe used in the biomedical

optical imaging system for *in situ* and *in vivo* minimally invasive diagnostic and/or guided surgery and treatment applications [19].

#### 4. Results and Discussion

For each sample in this study, optical intensity distribution data on the radial (i.e.,  $x$  and  $y$ ) planes were collected along the beam propagation (i.e., optical axial  $z$ ) direction from the plane of the first half peak intensity (beginning plane), through the maximum intensity plane, i.e., focus plane (center plane), to the second half peak intensity plane (end plane). Beam properties including working distance, spot size, and depth of field were analyzed by measured intensity distribution data with distance from the lens surface to the focal plane,  $1/e^2$  beam diameter at the focal plane, and the distance between the begin plane and the end plane, respectively. The measured results of the beam properties are listed in Table 1 along with detailed descriptions of the samples. The theoretical and experimental results of working distance, depth of focus, and spot size of various cases are shown in Figs. 2(a), 2(b), and 2(c) respectively, where dark lines represent the results using ray matrix transformation method, light lines represent results from ZEMAX simulations, and filled and empty points represent experimental results of samples with and without NCF.

For the samples without NCF, GRIN fiber lenses with a pitch range of 0.27 to 0.36 were directly attached to the SMF. From Fig. 2, both theoretical and experimental results demonstrate a low saturated value of working distance. For example, measured

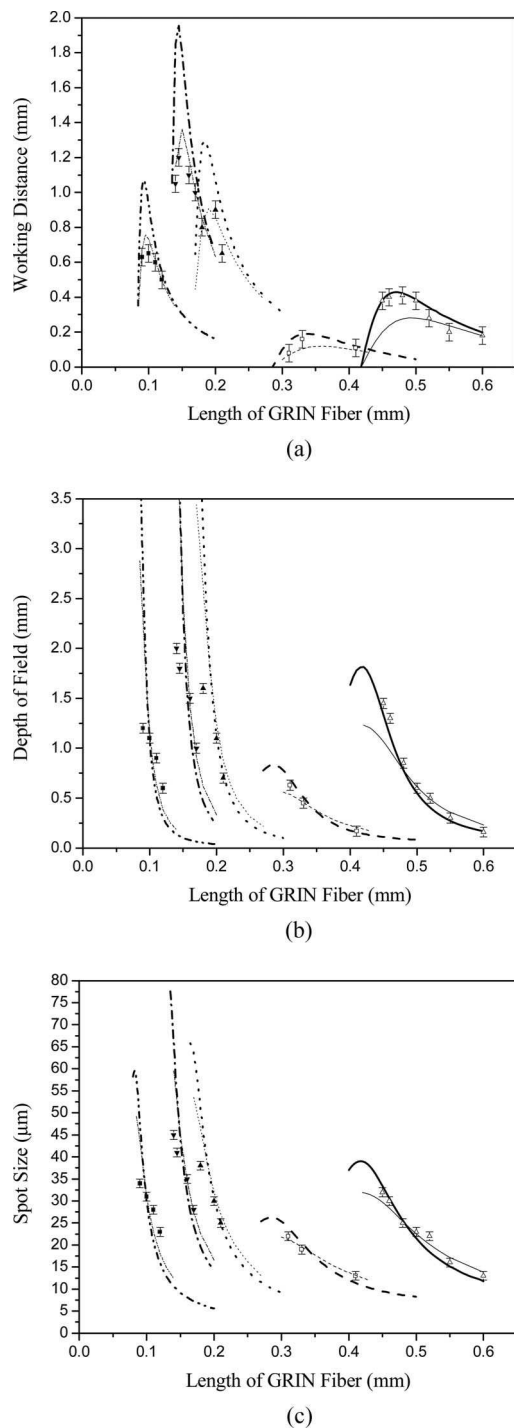


Fig. 2. Theoretical and experimental results of (a) working distance, (b) depth of field, and (c) spot size versus length of GRIN fiber, where dark and light lines represent the calculated results from the ray matrix transformation method and modeled results from ZEMAX at 1300 nm, solid and dash curves represent the samples of 100/140 and 50/125 GRIN fibers without NCF, dot and dash-dot curves represent the samples of 100/140 GRIN fiber with 0.36 and 0.48 mm NCF, and a dash-dot-dot curve represents the samples of 50/125 GRIN fiber with 0.36 mm NCF, respectively. The experimental results were represented as: hollow up-triangle and square points represent the samples of 100/140 and 50/125 GRIN fibers without NCF, filled up-triangle and down-triangle points represent the samples of 100/140 GRIN fiber with 0.36 and 0.48 mm NCF, and filled square points represents the samples of 50/125 GRIN fiber with 0.36 mm NCF, respectively.

saturated working distance was 0.16 and 0.41 mm at 0.29 pitch lens for 50/125 and 100/140 GRIN lenses, respectively. As discussed in the previous section, a small working distance of less than 0.4 mm is not suitable for most applications in biomedical imaging. Therefore, the probe built by directly attaching the GRIN lens to the SMF is less optimized for bioimaging applications, especially for the 50/125 lens, which had a working distance of less than 0.2 mm, although for the 100/140 lens, the depth of field reached 1.5 mm and spot size smaller than  $35 \mu\text{m}$ . A possible explanation for the small working distance can be attributed to the relatively large gradient constant  $g$  of the GRIN fiber lens in comparison to the glass GRIN lens. A smaller  $g$  produces a weaker focus ability, resulting in a longer working focus distance. Hence, the 100/140 GRIN fiber lens with  $g = 3.76$  is better than the 50/125 lens with  $g = 5.5$ , which is in good agreement with our results shown in Fig. 2(a). Unfortunately, for conventional GRIN fibers,  $g$  could not be further reduced.

From the theoretical result shown in Fig. 2(a), working distance could be increased by reducing the physical length of the GRIN fiber lens and, at the same time, by adding a piece of NCF between the SMF and the GRIN fiber lens to increase the mode field diameter of the input beam, thus, decreasing the focus ability of the GRIN fiber lens. The NCF was chosen to have the same material as the SMF in order to maintain the quality of the interface created by the fusion splicer. The lengths of the NCF used in this study were 0.36 mm for the 50/100 lens and 0.36 mm and 0.48 mm for 100/140 lenses. From our experimental results shown in Fig. 2, by adding a 0.36 mm long NCF fiber for both GRIN fiber lenses and reducing the GRIN fibers to around 0.1 mm (0.09 pitch) for the 50/125 GRIN lens and 0.2 mm (0.12 pitch) for the 100/140 GRIN lens, the working distances were noticeably increased. For the 50/125 GRIN fiber lens, the working distance was increased from 0.16 mm to 0.65 mm. By adding the same length of NCF to 100/140 GRIN fiber, the working distance was increased from 0.41 mm to 0.90 mm. Clearly, it was easier to achieve a longer working distance with the 100/140 GRIN fiber than the 50/125 GRIN fiber. By increasing the length of NCF to 0.48 mm and adjusting length of 100/140 GRIN fiber to 0.17 mm and 0.16 mm, the working distance reached to 1.0 mm and 1.1 mm, while the depth of field (0.95–1.5 mm) and spot sizes (28–35  $\mu\text{m}$ ) were still kept within a good range. The working distance could still be increased by further increasing the length of the NCF and decreasing relatively the length of the GRIN fiber lens. However, the working distance cannot be increased very much because as the working distance increases, the depth of field and spot size would be correspondingly increased, which would make the spot size large, thus decreasing the image resolution. By comparing the two theoretical methods, the results from the ZEMAX numerical optical design software were in better agreement with the experimental results than the analytic complex

beam parameter Gaussian matrix transformation method, although the latter method was in a better agreement in the case of a 100/140 GRIN fiber lens directly attached to SMF. Considering chromatic aberrations, we note the agreement between the experimental results with the broadband source and the ZEMAX simulations using a single wavelength. This demonstrates that the chromatic aberration of the lens is small. This is because the range of the zero-dispersion wavelengths,  $\{\lambda_0\}$ , of the used GRIN fibers is 1297–1316 nm. Furthermore, the zero-dispersion slope,  $S_0$ , for the used GRIN fibers is small in this band: equal to or smaller than 0.101 ps/nm<sup>2</sup>-km. Using the standard formula for dispersion in fiber,  $D(\lambda) = S_0[\lambda - \lambda_0^4/\lambda^3]/4$  (ps/nm-km), we calculated the changes in refractive index in the 1260–1370 nm wavelength range. By using these values in ZEMAX, we found out that for this range of wavelengths the relative changes of the working distance, depth of field, and spot size were all smaller than 3%.

Based on our results, the beam–distance profile for the application of optical biomedical imaging systems (i.e., 0.4–1.1 mm of focus distance, 0.8–1.5 mm of depth of field, and 26–35  $\mu\text{m}$  of spot size) can be obtained by combining a NCF and a GRIN fiber lens with lengths determined by the theoretical modeling. The technique described here possesses a high degree of flexibility for designing ultrasmall optical probes with different beam shapes for the different tissue imaging. The values of the numerical aperture (NA) of our lenses vary from 0.014 to 0.064, so they are considerably lower than the NA of any typical objective used in microscopy. Our NA values are low because of our choice to have a relatively long depth of field, thereby reducing variation in the spot size (i.e., lateral resolution) at different depths inside the sample.

A higher lateral resolution could be obtained by using larger probes with objectives of higher NA, but a dynamic focusing arrangement is required [23,24]. For example, in Ref. [23], a probe with 0.1 NA and a diameter of 5 mm is described. Due to the higher NA, the depth of field is only 0.08 mm and a micromotor is needed for dynamic focusing. The reported transverse resolution using this probe is approximately 8  $\mu\text{m}$ , but the dynamic focusing speed is limited to 100 Hz. In Ref. [24], a  $1.4 \times 1.0$  mm microelectromechanical membrane system (MEMS) is used for high-speed dynamic focusing. Because the MEMS had to be positioned at 45° angle between a collimator and an objective ( $f = 3.9$  mm, NA = 0.13), the probe diameter is larger than 6 mm. The reported transverse resolution is approximately 6.7  $\mu\text{m}$ . The sizes of these two higher NA probes are too large for *in vivo* imaging of small organs deep in the human body. Our probes have lower resolution than the previously reported higher NA ones, but have much smaller diameter (<150  $\mu\text{m}$ ), which make them ideal for *in vivo* imaging deep in the body.

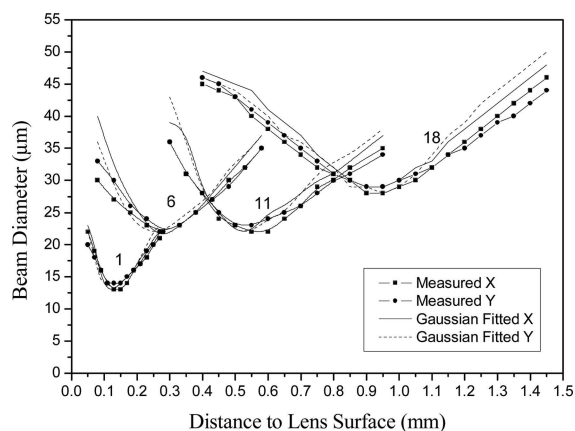
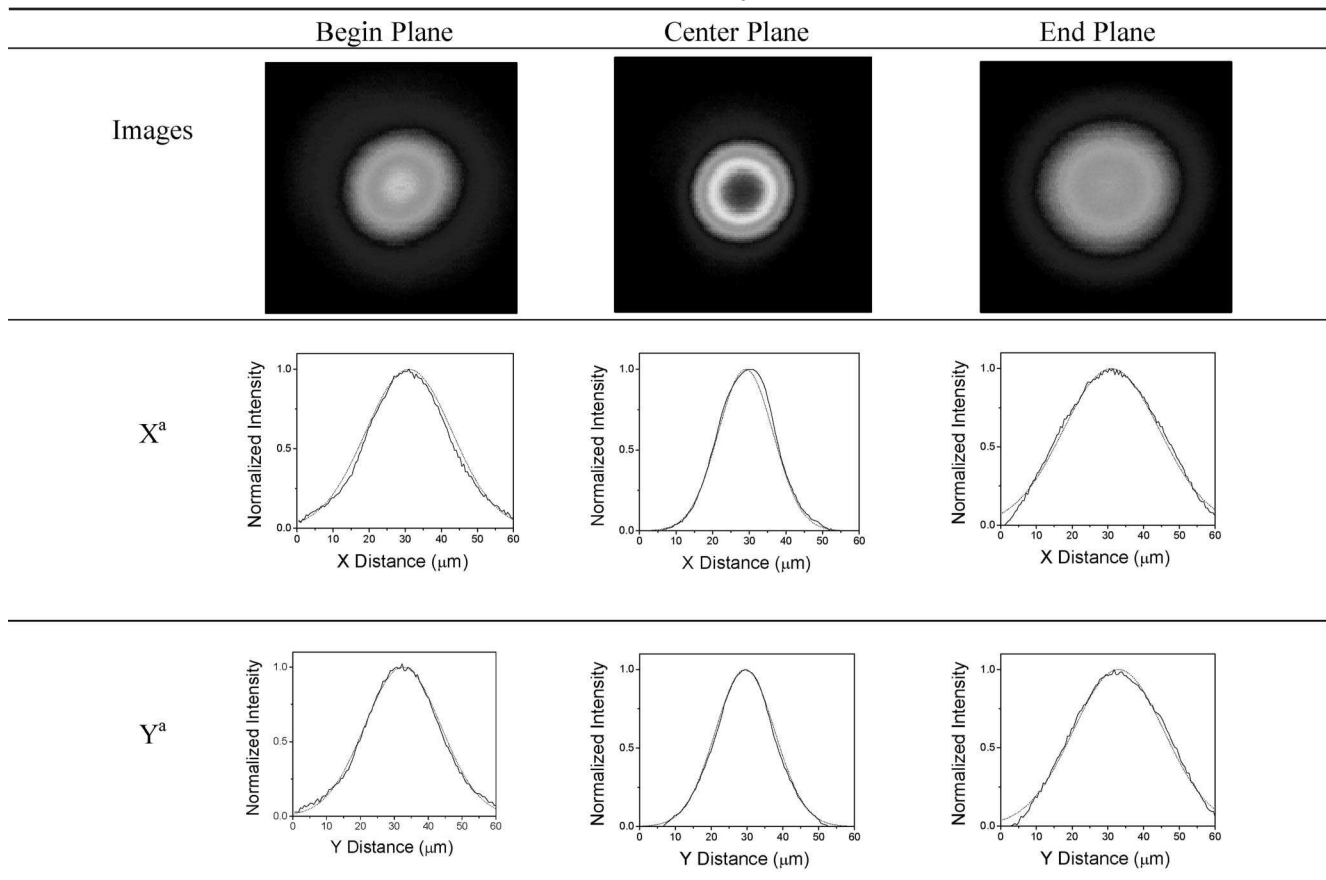


Fig. 3. Measured and Gaussian-fitted  $1/e^2$  intensity beam diameters along the axial distance (zero is the position of the lens surface) at  $x$  (horizontal) and  $y$  (vertical) radial coordination in the distance range of depth of field of the samples of 1, 6, 11, and 18.

Figure 3 shows measured and Gaussian-fitted  $1/e^2$  intensity beam diameters along the axial distance  $z$  (zero is the position of the lens surface) at  $x$  (horizontal) and  $y$  (vertical) radial coordination in the distance range of depth of field for four typical samples, i.e., samples 1 and 11 were made from the 50/125 GRIN fiber lens with and without NCF, and samples 6 and 18 were made from 100/140 GRIN fiber lens with and without NCF, respectively. In Fig. 3, for each curve, the smallest beam diameter value indicates spot size,  $x$ -coordinate value at the pole point indicates the working distance, and the distance range of the curve indicates the depth of field. From Fig. 3, the  $x$  and  $y$  symmetry of the beam diameter is very good for all samples. The measured beam diameters are well matched to Gaussian-fitted values in the center (focused) regions, but have small deviations on either side of the center region for some samples. Figure 3 also shows that working distance and depth of field are both increased by inserting a NCF; moreover, the spot sizes are also increased in accordance with the theory of Gaussian optics.

To further examine the beam properties of the lens system, Table 2 shows measured beam profile images and measured normalized intensity distributions with Gaussian-fitted results at the  $x$  and  $y$  directions on the three typical planes (i.e., begin plane, center plane, and end plane) of sample 18, the sample which had 0.17 mm length of 100/140 GRIN fiber lens with 0.48 mm NCF with working distance of 1.0 mm, depth of field of 0.95 mm, and spot size of 28  $\mu\text{m}$ . From the profile images and distributions shown in Table 2, the measured beam profiles match very well with Gaussian distributions at the beginning plane and center plane. On the end planes, the measured and Gaussian-fitted intensity distributions generally match very well despite slight deviations on both tail ends of the distributions leading to discrepancies between the measured and Gaussian-fitted beam diameters as was shown in Fig. 3. In addition, the circular shapes in the profile im-

Table 2. Measured Beam Profile Images and Normalized Intensity Distributions with Gaussian Fittings at  $x$  (Horizontal) and  $y$  (Vertical) Radial Coordination for Sample 18



<sup>a</sup>Solid curves represent measured results, and dashed curves represent their Gaussian fitting.

ages as shown in Table 2 indicate high  $x$  and  $y$  symmetry of the beam profiles through all the range of depth of field.

## 5. Conclusion

We presented a beam profile characterization of different variations of graded-index (GRIN) fiber lenses, which were recently proposed for ultrasmall biomedical imaging probes. Those GRIN lens modules were made of single mode fibers and GRIN fiber lenses with or without fiber spacers between them. We used fusion splicing between the fibers, lenses, and spacers to ensure high quality light transmission. We verified experimentally that the insertion of a NCF between the SMF and the GRIN fibers is an efficient way to increase the working distance of the probe, while preserving an appropriate depth of field and spot size. We also found that beam-distance profiles (i.e., 0.4–1.1 mm of focus distance, 0.8–1.5 mm of depth of field, and 26–35  $\mu\text{m}$  of spot size) can be obtained by adjusting the lengths of the NCF and the GRIN fiber lens for the different tissue imaging. By implementing modules with two different GRIN fibers, we demonstrated that it is easier to achieve a longer working distance for a GRIN fiber with lower value of gradient constant  $g$  than with a higher one. Using ZEMAX,

optical design software, we modeled our optic probes, which proved a more precise approach than the results obtained by the analytic Gaussian matrix transformation method. We obtained very high quality focused Gaussian beam profiles with high  $x$  and  $y$  symmetry using the conventional multimode GRIN fibers. Their high quality beam and ultrasmall size make such GRIN lens based probes very valuable for biomedical optical imaging systems.

Youxin Mao gratefully thanks Alex Vitkin, Victor Yang, and Xijia Gu for their encouragement, Erroll Murdock and Jianzhao Li for their experimental assistance, and Man F. Yan, OFS Laboratories, Murray Hill, New Jersey, USA, for supplying the 50/125 GRIN fiber.

## References

1. D. Huang, E. A. Swanson, C. P. Lin, J. S. Schuman, W. G. Stinson, W. Chang, M. R. Hee, T. Flotte, K. Gregory, C. A. Puliafito, and J. G. Fujimoto, "Optical coherence tomography," *Science* **254**, 1178–1181 (1991).
2. Z. P. Chen, T. E. Milner, D. Dave, and J. S. Nelson, "Optical Doppler tomographic image of fluid flow velocity in highly scattering media," *Opt. Lett.* **22**, 64–66 (1997).
3. J. A. Izatt, M. D. Kulkarni, S. Yazdanfar, J. K. Barton, and A. J. Welch, "In vivo bidirectional color Doppler flow imaging

- of picoliter blood volumes using optical coherence tomography,” *Opt. Lett.* **22**, 1439–1441 (1997).
4. S. Yazdanfar, A. M. Rollins, and J. A. Izatt, “Ultrahigh-velocity resolution imaging of the microcirculation *in vivo* using color Doppler optical coherence tomography,” *Proc. SPIE* **4251**, 156–164 (2001).
  5. V. X. D. Yang, M. L. Gordon, B. Qi, J. Pekar, S. Lo, E. Seng-Yue, A. Mok, B. C. Wilson, and I. A. Vitkin, “High speed, wide velocity dynamic range Doppler optical coherence tomography (Part I): system design, signal processing, and performance,” *Opt. Express* **11**, 794–809 (2003).
  6. B. R. White, M. C. Pierce, N. Nassif, B. Cense, B. H. Park, G. J. Tearney, B. E. Bouma, T. C. Chen, and J. F. de Boer, “*In vivo* dynamic human retinal blood flow imaging using ultra-high-speed spectral domain optical coherence tomography,” *Opt. Express* **11**, 3490–3497 (2003).
  7. S. Yazdanfar, A. M. Rollins, and J. A. Izatt, “Imaging and velocimetry of the human retinal circulation with color Doppler optical coherence tomography,” *Opt. Lett.* **25**, 1448–1450 (2000).
  8. Y. H. Zhao, Z. P. Chen, C. Saxer, S. H. Xiang, J. F. de Boer, and J. S. Nelson, “Phase-resolved optical coherence tomography and optical Doppler tomography for imaging blood flow in human skin with fast scanning speed and high velocity sensitivity,” *Opt. Lett.* **25**, 114–116 (2000).
  9. Y. Zhao, Z. P. Chen, C. Saxer, Q. Shen, S. Xiang, J. F. de Boer, and J. S. Nelson, “Doppler standard deviation imaging for clinical monitoring of *in vivo* human skin blood flow,” *Opt. Lett.* **25**, 1358–1360 (2000).
  10. V. X. D. Yang, S. Tang, M. L. Gordon, B. Qi, G. Gardiner, M. Cirocco, P. Kortan, G. Haber, G. Kandel, I. A. Vitkin, and B. C. Wilson, “Endoscopic Doppler optical coherence tomography in human gastrointestinal tract: initial experience,” *Gastrointest. Endosc.* **61**, 879–890 (2005).
  11. P. H. Tran, D. S. Mukai, M. Brenner, and Z. Chen, “*In vivo* endoscopic optical coherence tomography by use of a rotational microelectromechanical system probe,” *Opt. Lett.* **29**, 1236–1238 (2004).
  12. X. Li, C. Chudoba, T. Ko, C. Pitris, and J. G. Fujimoto, “Imaging needle for optical coherence tomography,” *Opt. Lett.* **25**, 1520–1522 (2000).
  13. V. X. D. Yang, Y. X. Mao, N. Munce, B. Standish, W. Kucharczyk, N. E. Marcon, B. C. Wilson, and I. A. Vitkin, “Interstitial Doppler optical coherence tomography,” *Opt. Lett.* **30**, 1791–1793 (2005).
  14. J. G. Fujimoto, S. A. Bopart, G. J. Tearney, B. E. Bouma, C. Pitris, and M. E. Brezinski, “High resolution *in vivo* intra-arterial imaging with optical coherence tomography,” *Heart* **82**, 128–133 (1999).
  15. L. J. Diaz-Sandoval, B. E. Bouma, G. J. Tearney, and I. Jang, “Optical coherence tomography as a tool for percutaneous coronary interventions,” *Catheter. Cardio. Interv.* **65**, 492–496 (2005).
  16. E. Swanson, C. L. Petersen, E. McNamara, R. B. Lamport, and D. L. Kelly, “Ultrasmall optical probes, imaging optics, and methods for using same,” U.S. Patent 6445939 (3 September 2002).
  17. W. A. Reed, M. F. Yan, and M. J. Schnitzer, “Gradient-index fiber-optic microprobes for minimally invasive *in vivo* low-coherence interferometry,” *Opt. Lett.* **27**, 1794–1796 (2002).
  18. M. S. Jafri, S. Farhang, R. S. Tang, N. Desai, P. S. Fishman, R. G. Rohwer, C. Tang, and J. M. Schmitt, “Optical coherence tomography in the diagnosis and treatment of neurological disorders,” *J. Biomed. Opt.* **10**(5), 051603 (2005).
  19. H. Li, B. A. Standish, A. Mariampillai, N. R. Munce, Y. Mao, S. Chiu, N. E. Marcon, B. C. Wilson, A. Vitkin, and V. X. D. Yang, “Feasibility of interstitial Doppler optical coherence tomography for *in vivo* detection of microvascular changes during photodynamic therapy,” *Lasers Surgery Med.* **38**, 754–761 (2006).
  20. A. W. Sainter, T. A. King, and M. R. Dickinson, “Theoretical comparison of light sources for use in optical coherence tomography,” *Proc. SPIE* **4619**, 289–299 (2002).
  21. H. W. Kogelnik and T. Li, “Laser beam and resonators,” *Appl. Opt.* **5**, 1550 (1966).
  22. W. L. Emkey and C. A. Jack, “Analysis and evaluation of graded-index fiber-lenses,” *J. Lightwave Technol.* **LT-5**, 1156–1164 (1987).
  23. P. R. Herz, Y. Chen, A. D. Aguirre, K. Schneider, P. Hsiung, and J. G. Fujimoto, “Micromotor endoscope catheter for *in vivo*, ultrahigh-resolution optical coherence tomography,” *Opt. Lett.* **29**, 2261–2263 (2004).
  24. V. X. D. Yang, Y. Mao, B. A. Standish, N. Munce, S. Chiu, D. Burnes, B. C. Wilson, I. A. Vitkin, P. A. Himmer, and D. L. Dickensheets, “Doppler optical coherence tomography with a micro-electro-mechanical membrane mirror for high-speed dynamic focus tracking,” *Opt. Lett.* **31**, 1262–1264 (2006).